

1-1-2023

Strong and ductile Al–Mn–Mg–Sc–Zr alloy achieved in fabrication-rate enhanced laser powder bed fusion

Hao Zhang

Lai Chang Zhang
Edith Cowan University

Hongyu Liu

Xiaodong Niu

Marcus C. Lam

See next page for additional authors

Follow this and additional works at: <https://ro.ecu.edu.au/ecuworks2022-2026>



Part of the [Engineering Commons](#)

[10.1080/17452759.2023.2250769](https://doi.org/10.1080/17452759.2023.2250769)

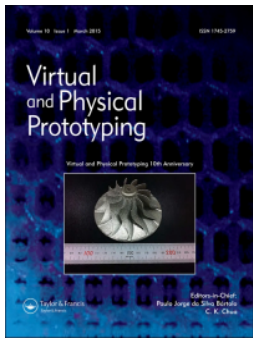
Zhang, H., Zhang, L. C., Liu, H., Niu, X., Lam, M. C., Zhang, W., ... & Cao, S. (2023). Strong and ductile Al–Mn–Mg–Sc–Zr alloy achieved in fabrication-rate enhanced laser powder bed fusion. *Virtual and Physical Prototyping*, 18(1), e2250769. <https://doi.org/10.1080/17452759.2023.2250769>

This Journal Article is posted at Research Online.

<https://ro.ecu.edu.au/ecuworks2022-2026/3041>

Authors

Hao Zhang, Lai Chang Zhang, Hongyu Liu, Xiaodong Niu, Marcus C. Lam, Wenzhe Zhang, Xiaojie Jin, Fuzhong Chu, Xinhua Wu, and Sheng Cao



Strong and ductile Al–Mn–Mg–Sc–Zr alloy achieved in fabrication-rate enhanced laser powder bed fusion

Hao Zhang, Lai-Chang Zhang, Hongyu Liu, Xiaodong Niu, Marcus C. Lam, Wenzhe Zhang, Xiaojie Jin, Fuzhong Chu, Xinhua Wu & Sheng Cao

To cite this article: Hao Zhang, Lai-Chang Zhang, Hongyu Liu, Xiaodong Niu, Marcus C. Lam, Wenzhe Zhang, Xiaojie Jin, Fuzhong Chu, Xinhua Wu & Sheng Cao (2023) Strong and ductile Al–Mn–Mg–Sc–Zr alloy achieved in fabrication-rate enhanced laser powder bed fusion, *Virtual and Physical Prototyping*, 18:1, e2250769, DOI: [10.1080/17452759.2023.2250769](https://doi.org/10.1080/17452759.2023.2250769)

To link to this article: <https://doi.org/10.1080/17452759.2023.2250769>



© 2023 The Author(s). Published by Informa UK Limited, trading as Taylor & Francis Group



[View supplementary material](#)



Published online: 29 Aug 2023.



[Submit your article to this journal](#)



Article views: 704



[View related articles](#)



[View Crossmark data](#)

Strong and ductile Al–Mn–Mg–Sc–Zr alloy achieved in fabrication-rate enhanced laser powder bed fusion

Hao Zhang^a, Lai-Chang Zhang^b, Hongyu Liu^c, Xiaodong Niu^c, Marcus C. Lam^d, Wenzhe Zhang^e, Xiaojie Jin^f, Fuzhong Chu^g, Xinhua Wu^{a,f} and Sheng Cao^c

^aFaculty of Materials and Manufacturing, Beijing University of Technology, Beijing, People's Republic of China; ^bCentre for Advanced Materials and Manufacturing, School of Engineering, Edith Cowan University, Perth, Australia; ^cDepartment of Mechanical Engineering, College of Engineering, Shantou University, Shantou, People's Republic of China; ^dDepartment of Materials Science and Engineering, Monash University, Clayton, Australia; ^eDepartment of Materials Science and Engineering, Southeast University, Nanjing, People's Republic of China; ^fAmPro Innovations Co., Ltd., Suzhou, People's Republic of China; ^gARC Research Hub for Computational Particle Technology, Department of Chemical and Biological Engineering, Monash University, Clayton, Australia

ABSTRACT

The high cost of laser powder bed fusion (LPBF) fabricated high-strength Sc containing aluminium alloy hinders its applications. To reduce the cost, we reported a LPBF fabricated strong and ductile Al–Mn–Mg–Sc–Zr alloy using large layer thicknesses to improve the fabrication efficiency on coarse powder particles. A high relative density exceeding 99.2% was achieved at layer thicknesses up to 120 µm. In post-process heat-treated specimens, the yield strength only had a slight 6% decrease from layer thickness of 30 to 120 µm; such a decrease in strength was attributed to the larger grain size resulted from the adopted larger layer thickness. The fabricated sample at layer thickness of 120 µm still exhibited high tensile yield strength of 472 MPa and fracture strain of ~10%. This work showed a successful application of improving the LPBF fabrication efficiency of high-strength Al–Mn–Mg–Sc–Zr alloy using large layer thickness in LPBF process.

ARTICLE HISTORY

Received 25 April 2023
Accepted 17 August 2023

KEYWORDS





Al–Mn–Mg–Sc–Zr alloy; laser powder bed fusion; fabrication rate; layer thickness; high strength


1. Introduction

The emerging additive manufacturing (AM) technique is known for advantages of high geometric manufacturing freedom and high levels of product customisation [1–4]. As an AM technology, laser powder bed fusion (LPBF) uses a high-energy laser beam to selectively melt metallic powder layers successively in a protective atmosphere until the whole component is completely built [5]. The LPBF fabricated aluminium alloys combine excellent properties of high specific strength, good corrosion resistance, and outstanding processability, which have been extensively used in a wide range of industrial sectors [6–9]. However, the majority of widely employed LPBF fabricated aluminium alloys, i.e. AlSi7Mg, AlSi10Mg and AlSi12, exhibit low strength with ultimate tensile strength (UTS) of <400 MPa, which limits their industrial applications. In contrast, LPBF fabricated high-strength 2xxx [10], 5xxx [11], 6xxx [12] and 7xxx [13] series aluminium alloys are susceptible to hot cracks during the fast solidification in the process of LPBF, and these high-strength

aluminium alloys are not suitable for fabrication by LPBF. Therefore, developing fabricable crack-free high-strength aluminium alloys for LPBF process has attracted extensive attention in recent years [14–22].

For LPBF fabricated high-strength aluminium alloys, Wang et al. [23] reported a LPBF fabricated and post heat treated Al–Cu–Mg–Si alloy with an UTS of 455 MPa. In addition, another work on Zr-modified high-strength Al–Cu–Mg alloy showed crack-free microstructure after LPBF manufacturing and a high UTS of 424 MPa [24]. Although these LPBF fabricated crack-free aluminium alloys do exhibit good mechanical properties, their work-hardening behaviours are not satisfactory. In contrast, the recently developed high-strength Al–Mn–Mg–Sc–Zr alloy (with supersaturated Mn and Sc, Zr additions) has showed its LPBF printability (crack-free), a UTS of 560 MPa (the highest one in literature), and an exceptional work-hardening behaviour [25,26]. The high strength was achieved by a simple post-heat-treatment at 300°C for 5 h. Such a heat treatment resulted in

CONTACT Sheng Cao  sheng.cao@foxmail.com  Department of Mechanical Engineering, College of Engineering, Shantou University, Shantou 515063, China; Lai-chang Zhang  l.zhang@ecu.edu.au  Centre for Advanced Materials and Manufacturing, School of Engineering, Edith Cowan University, 270 Joondalup Drive, Joondalup, Perth, Western Australia 6027, Australia

 Supplemental data for this article can be accessed online at <https://doi.org/10.1080/17452759.2023.2250769>.

This article has been corrected with minor changes. These changes do not impact the academic content of the article.

© 2023 The Author(s). Published by Informa UK Limited, trading as Taylor & Francis Group

This is an Open Access article distributed under the terms of the Creative Commons Attribution-NonCommercial License (<http://creativecommons.org/licenses/by-nc/4.0/>), which permits unrestricted non-commercial use, distribution, and reproduction in any medium, provided the original work is properly cited. The terms on which this article has been published allow the posting of the Accepted Manuscript in a repository by the author(s) or with their consent.

Table 1. Chemical composition (wt. %) of Al–Mn–Mg–Sc–Zr powder particle used in this work.

Material	Al	Mn	Mg	Sc	Zr	Si	Fe
Al–Mn–Mg–Sc–Zr	Bal.	3.04	1.60	0.78	0.22	0.06	0.06

a matrix supersaturated in Mn and the formation of nano Al_3Sc particles, which contributed to solid solution strengthening, grain refinement strengthening, and precipitation strengthening [5, 27–30].

However, the cost of LPBF fabricated high-strength Al–Mn–Mg–Sc–Zr alloy is high due to the expensive Sc addition and the low layer-by-layer forming efficiency corresponding to the small layer thickness at 30 μm [7, 31–34]. In addition, the cost of powder particles depends on the size, and fine particles are much more expensive than the coarse counterparts in additive manufacturing applications [35–37]. The high cost hinders the applications of LPBF fabricated high-strength aluminium alloys.

Therefore, the current work aimed to employ a large LPBF layer thickness on coarse high-strength Al–Mn–Mg–Sc–Zr alloy powder particles to increase the productivity and to reduce the fabrication cost. Systematic processing optimisation was conducted in different layer thicknesses of 30, 60, 90, and 120 μm , and the processing windows were obtained in these layer thicknesses. In addition, the specimen quality, microstructure, and mechanical properties were carefully investigated. A strong and ductile high strength aluminium alloy was achieved in the 120 μm layer thickness condition with yield strength (YS) of 472 MPa and the fracture strain of $\sim 10\%$.

2. Materials and methods

2.1. Materials and LPBF fabrication

The pre-alloyed Al–Mn–Mg–Sc–Zr powder with a nominal composition listed in Table 1 was prepared by

Hunan Dongfang scandium Industry Co., Ltd., using gas atomisation. Figure 1 shows the powder particle morphology and its size distribution. These powder particles were generally spherical, and the particle size distribution was from ~ 6 to ~ 100 μm with D_{10} , D_{50} and D_{90} at 15.7, 31.7 and 69.2 μm , respectively.

The LPBF fabrication was carried out using an Ampro SP260 LPBF machine equipped with a 500 W fibre laser with a spot size of 70 μm in a protective argon atmosphere. Specimens were built on a preheated substrate at 100°C using various laser powers and scan speeds, which were in the range of 200–450 W and 800–2000 mm/s, respectively. For all specimens, a strip scan strategy with a scanning rotation of 67° between the consecutive layers was used, and the hatch distance was 140 μm . The LPBF fabrication was performed at different layer thicknesses of 30, 60, 90, and 120 μm . These samples were post-process heat treated in a muffle furnace in air at 300°C for 5 h for microstructure characterisations and tensile tests.

2.2. Microstructural characterisations and tensile tests

The samples for microstructural and hardness characterisations were ground to a 5000-grit finish using SiC papers, which were then polished using a suspension of 50 nm SiO_2 Nano-MAX. The specimen quality was examined by an optical microscope (OM, DT2000, Beijing Xinliyang Technology & Development Co. Ltd.). A DH-200M density instrument was used to measure the relative density of the as-built samples according to the Archimedes principle. In addition, samples were etched by a Keller's reagent (which was composed of 2.5 mL HNO_3 , 1.5 mL HCl , 1 mL HF and 95 mL deionised water) to reveal the melt pool morphology. To further validate the relative density results, two extreme conditions fabricated at 30 and 120 μm layer thicknesses were examined using a

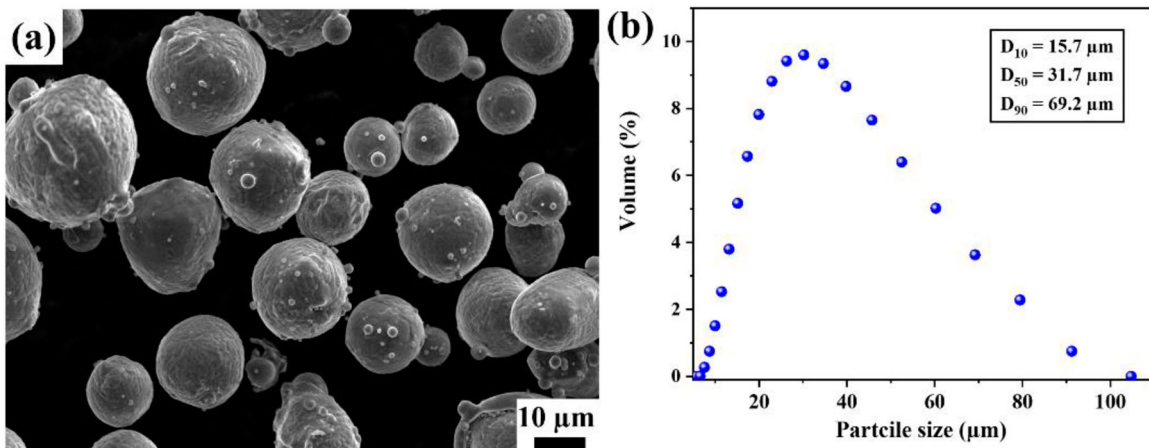


Figure 1. (a) Secondary electron (SE) SEM image showing the powder particle morphology and (b) the particle size distribution of the pre-alloyed Al–Mn–Mg–Sc–Zr powder.

micro-CT (μ -CT) system (FF85, Comet Yxlon Ltd.,) with a tube voltage of 180 kV, a current of 130 μ A, a focus size of 4 μ m, a voxel size of ~ 5.6 μ m and a filter of 1 mm.

A field emission scanning electron microscope (SEM, JSM-7200F, Japan JEOL, Ltd., Japan) was used to observe the morphology of powder particles and post heat treated specimen microstructure. A Zeiss Gemini 300 SEM equipped with a backscatter electron (BSE) detector and an electron backscatter diffraction (EBSD, EDAX Velocity Super) system was used to characterise the microstructure and determine the grain orientations. For transmission electron microscopy (TEM) and scanning TEM (STEM) characterisation, specimens with a 3 mm in diameter were mechanically ground to 150 μ m thick and then ion milled using a Gatan 691 ion polishing system at an angle of 5° and a voltage of 3.6 keV. TEM (FEI Tecnai F30) experiments were then applied to determine the nanoscale microstructure of the post-heat-treated samples to obtain bright field (BF) images, high angle annular dark field (HAADF) images, and energy dispersive X-ray spectra (EDS) maps.

As this work employed strategies of using large layer thickness to improve the LPBF productivity, only vertically built specimens with the loading direction parallel to the LPBF build direction were included in the tensile test to examine the inter-layer bond. For the room temperature tensile test, M10 cylindrical specimens with a gauge diameter of 6 mm and a gauge length of 24 mm were used according to the ASTM E8 standard. Tensile tests were carried out on a GNT-50 machine equipped with a 10 mm extensometer at a constant crosshead moving speed of 1 mm/min. For each layer

thickness condition, three tensile replicates were separately tested. After tensile tests, fractographic examinations were conducted on a JSM-7200F SEM.

3. Results

3.1. Specimen density and defects at different LPBF layer thicknesses

Figure 2 shows the representative OM images of the as-built samples at different LPBF layer thicknesses. At all layer thickness adopted in this work, excessive fusion (highlighted by yellow dashed lines) with some keyholes defects was observed in processing conditions of high laser powers and low scan speeds, and irregular lack-of-fusion defects (highlighted by green dashed lines) occurred when low laser powers and high scan speeds were applied. Between the excessive and insufficient fusions, optimised processing windows (highlighted by red dashed lines) without apparent defects were obtained in all layer thickness conditions. With increased layer thickness, the processing window became narrower. The optimised laser power range was increased from 270–370 W at 30 μ m layer thickness to 400–450 W at 120 μ m layer thickness. This is attributed to that an increased laser power was required to melt a larger volume of powder resulted from an enhanced layer thickness. Table 2 lists three processing parameter sets with the highest relative density for different LPBF layer thicknesses. For energy density of specimens

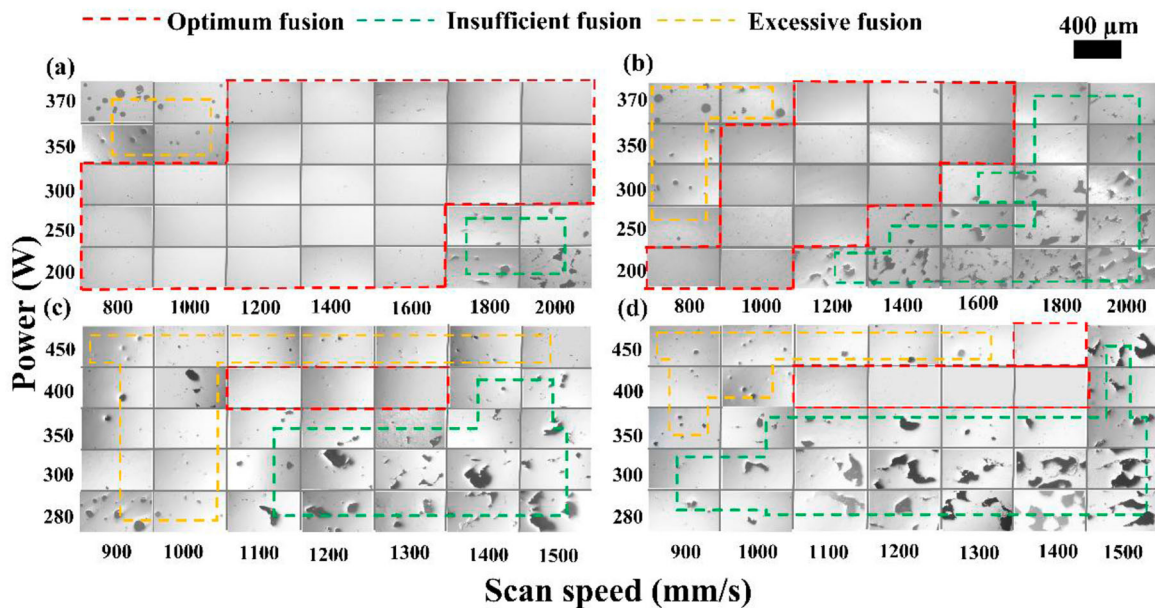


Figure 2. Representative optical micrographs of Al-Mn-Mg-Sc-Zr samples fabricated at different LPBF layer thickness of: (a) 30 μ m, (b) 60 μ m, (c) 90 μ m, and (d) 120 μ m.

Table 2. The three processing parameter sets with the highest relative density measured by the Archimedes principle for Al–Mn–Mg–Sc–Zr samples fabricated at different LPBF layer thickness.

Layer thickness (μm)	Laser power (W)	Scanning speed (mm/s)	Volumetric energy density (J/mm^3)	Relative density (%)
30	350	1200	64.9	99.8 ± 0.1
	350	1400	59.5	99.5 ± 0.2
	300	1200	59.5	99.1 ± 0.2
60	370	1200	36.7	99.7 ± 0.1
	350	1200	34.7	99.4 ± 0.3
	300	1000	35.7	99.2 ± 0.4
90	400	1200	26.4	99.5 ± 0.3
	400	1100	28.8	99.1 ± 0.3
	400	1300	24.4	98.9 ± 0.5
120	400	1100	21.6	99.3 ± 0.3
	450	1400	19.1	98.9 ± 0.5
	400	1200	19.8	98.6 ± 0.3

listed in Table 2, the overall trend of volumetric energy density decreased with enhanced layer thickness.

For different LPBF layer thicknesses, the samples with the highest relative density were used for subsequent microstructure characterisation and mechanical tests. Hereafter, the 30 μm specimen refers to 350 W and 1200 mm/s, the 60 μm specimen is 370 W and 1200 mm/s, the 90 μm specimen corresponds to 400 W and 1200 mm/s, and the 120 μm specimen is built at 400 W

and 1100 mm/s. To further validate the relative density measured by the Archimedes method, two specimens in the extreme layer thickness values of 30 and 120 μm were characterised by $\mu\text{-CT}$ analysis. Figure 3 shows the reconstructed 3D visualisations and vertical cross-sections of the $\mu\text{-CT}$ results. No cracks and irregular defects were observed in both specimens. More specifically, there were no apparent pores in the specimen built at layer thickness of 30 μm (99.8% relative density), while some pores were observed in the specimen built at layer thickness of 120 μm (99.2% relative density). These defects in the 120 μm specimen were related to the increased laser power and associated keyhole and gas pore formation. The relative density measured by $\mu\text{-CT}$ is consistent with the Archimedes measurement for these two specimens.

3.2. Melt pool characteristics

Figure 4 illustrates the melt pool morphology of specimens built at different layer thickness. In the 30 μm specimen, there were only a few defects with dark contrast. The amount and size of defects increased with the layer thickness adopted for the LPBF process. This result is consistent with the above $\mu\text{-CT}$ results (Figure 3). In addition, melt pools became wider and deeper at larger layer thickness.

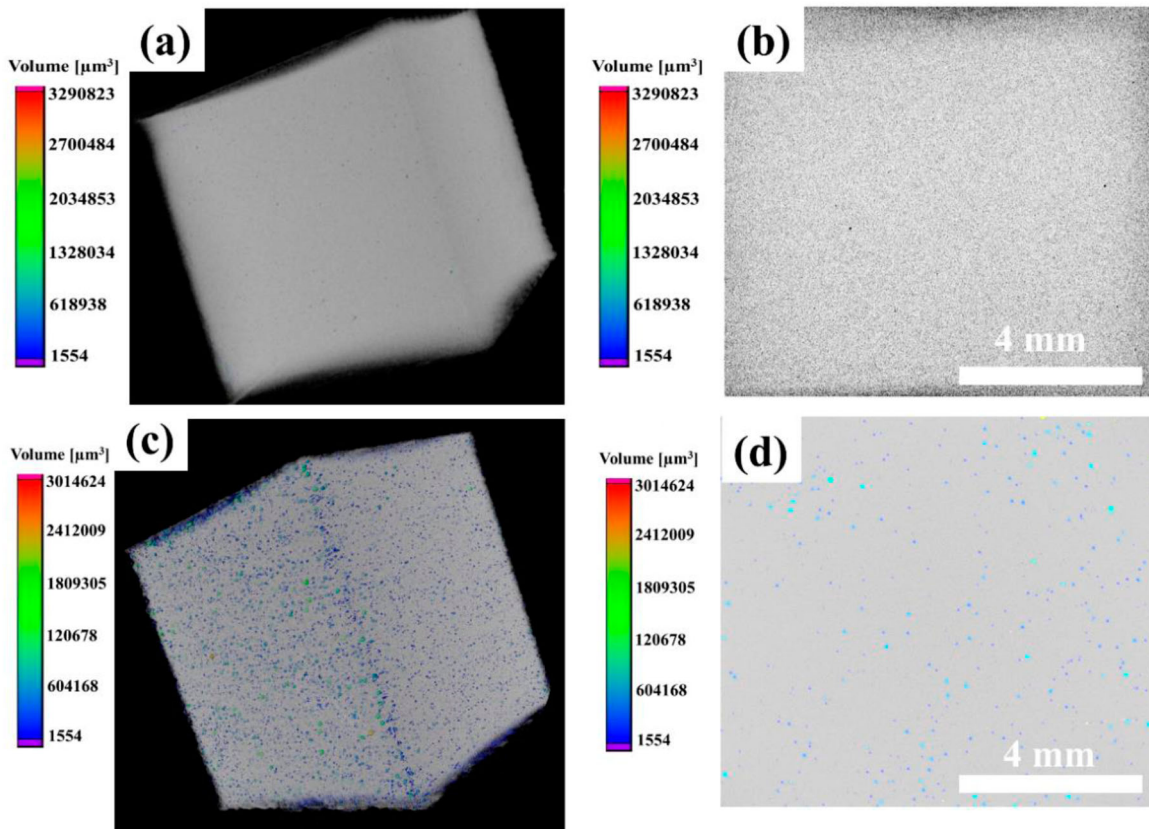


Figure 3. Defects in LPBF fabricated samples (10 mm \times 10 mm \times 10 mm) in 3D visualisation (a and c) and observed along a vertical projection (b and d) revealing the pore morphology and distribution reconstructed from the $\mu\text{-CT}$ images of (a–b) 30 μm (350 W, 1200 mm/s) and (c–d) 120 μm (400 W, 1100 mm/s) specimens. The voxel size was approximately at 5.6 μm .

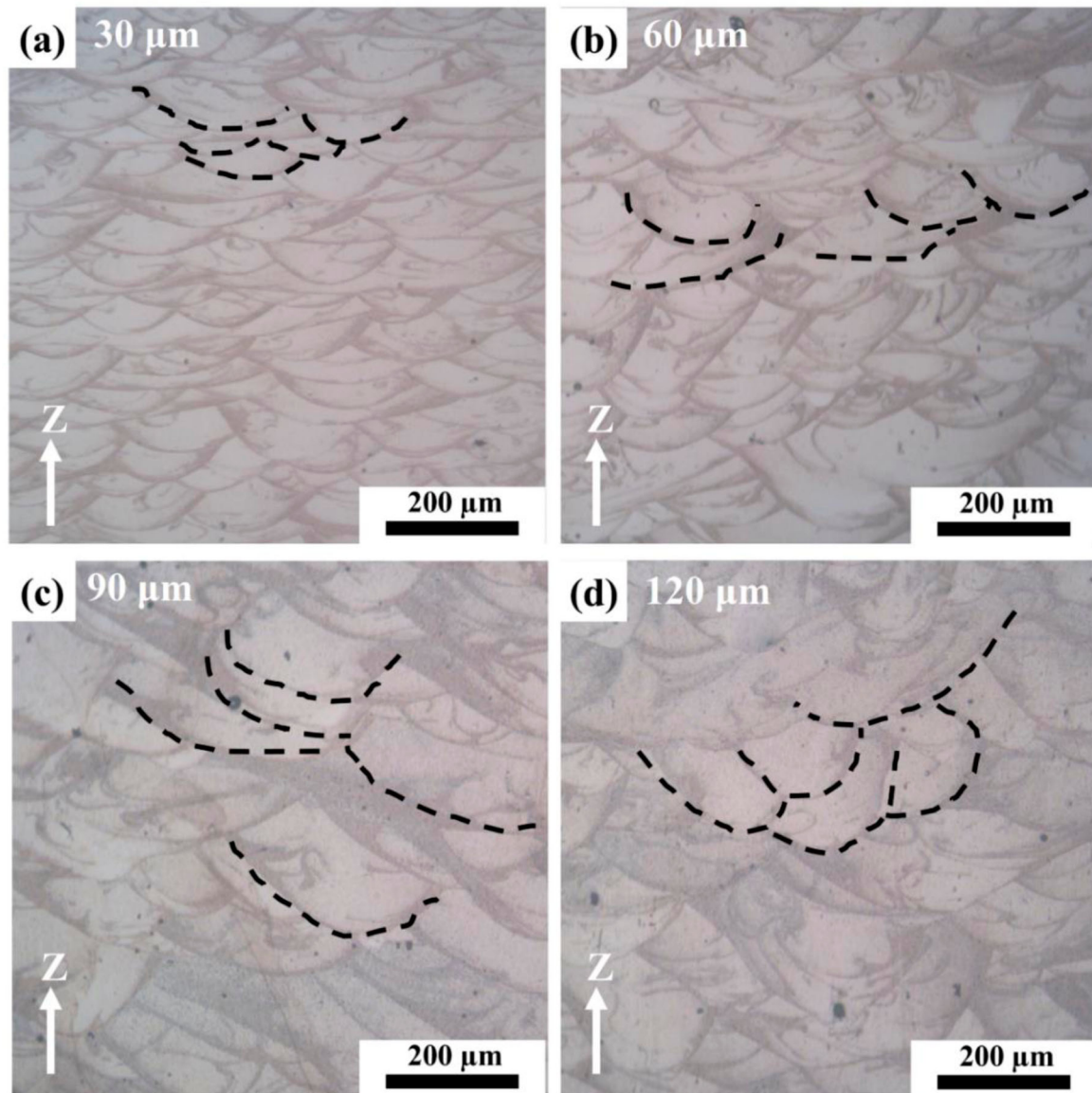


Figure 4. The morphology of melt pool in Al-Mn-Mg-Sc-Zr alloy specimens built at different LPBF layer thickness of: (a) 30 μm , (b) 60 μm , (c) 90 μm , and (d) 120 μm .

After analysing 10 OM images at each thickness condition, the melt pool width, depth, and depth to width ratio are summarised in Figure 5. The width of the melt pool at 30, 60, 90, and 120 μm layer thickness was 170, 205, 234, and 212 μm , respectively. The depth of melt pool was 51, 89, 95, and 105 μm for 30, 60, 90, and 120 μm layer thickness, respectively. In addition, the depth-to-width ratio was 0.3, 0.5, 0.4 and 0.6 for 30, 60, 90, and 120 μm layer thickness, respectively.

3.3. Microstructure analysis

Figure 6 shows the microstructure of post-heat-treated Al-Mn-Mg-Sc-Zr alloys built at different LPBF layer thickness. All the four specimens exhibited a heterogeneous

microstructure composed of small equiaxed grains (EG) at the melt pool boundary and large columnar grains (CG) within the melt pool. Such a heterogeneous microstructure was widely reported in LPBF fabricated alloys [38]. EBSD experiments were conducted to obtain grain orientation maps of these specimens. To show the heterogeneous columnar and equiaxed grains, grain orientation maps were collected on the vertical cross-sections, as shown in Figure 7. The EBSD observed heterogeneous microstructure was similar to the SEM images in Figure 6. There were some black-coloured regions at melt pool boundaries in the grain orientation maps, which were fine grains under the EBSD resolution. With an enhanced layer thickness, the grains seemed to become coarser. In addition, the area fractions of EG and CG regions varied at different LPBF layer thickness.

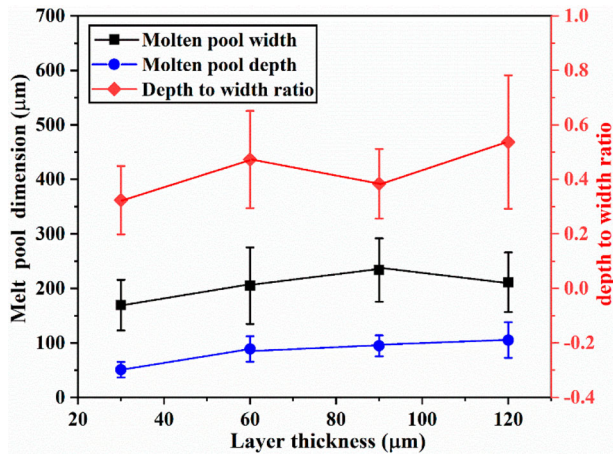


Figure 5. The melt pool width, depth, and depth to width ratio of the LPBF fabricated Al-Mn-Mg-Sc-Zr specimens built at different LPBF layer thickness.

The fraction of EG increased and the fraction of CG decreased with the layer thickness. As shown in Table 3, the fractions of EG and CG in 30, 60, 90 and 120 μm specimens were 20.1%, 22.4%, 28.3% and 29.4%, respectively and 79.9%, 77.6%, 71.3% and 70.6%, respectively.

To reveal the intergranular and intragranular structures, the STEM EDS mapping was used to analyse large sized precipitates. As shown in Figure 8(a)–(h), there were Mn-enriched and Sc-enriched precipitates in the EG region. The Sc-rich particles showed a cube-shape morphology with a fuzzy contrast and the (Mn, Fe)-rich particles had a bright contrast. In addition, Mg_2Si precipitates with a dark contrast were observed in the STEM image. These three types of precipitates were also previously reported in literature [19, 26]. According to previous studies, the Mn and Fe enriched precipitates should be $Al_6(Mn, Fe)$, and the Sc enriched precipitates should be the primary Al_3X (Al_3Sc and/or $Al_3(Sc, Zr)$) [28].

In a previous study, Vlach et al. [39] found that the formation $Al_6(Mn, Fe)$ had no significant effect on the hardness of aging treated Al-Si-Mg-Mn alloy with additions of Sc and Zr. In addition, the grain size of EGs and CGs increased with layer thickness (Figure S1 in the supplemental material), and their grain sizes are summarised in Table 3. Such a difference in microstructure at various layer thickness should be related to the different thermal history associated with the changed layer thickness, which will be discussed in Section 4.3.

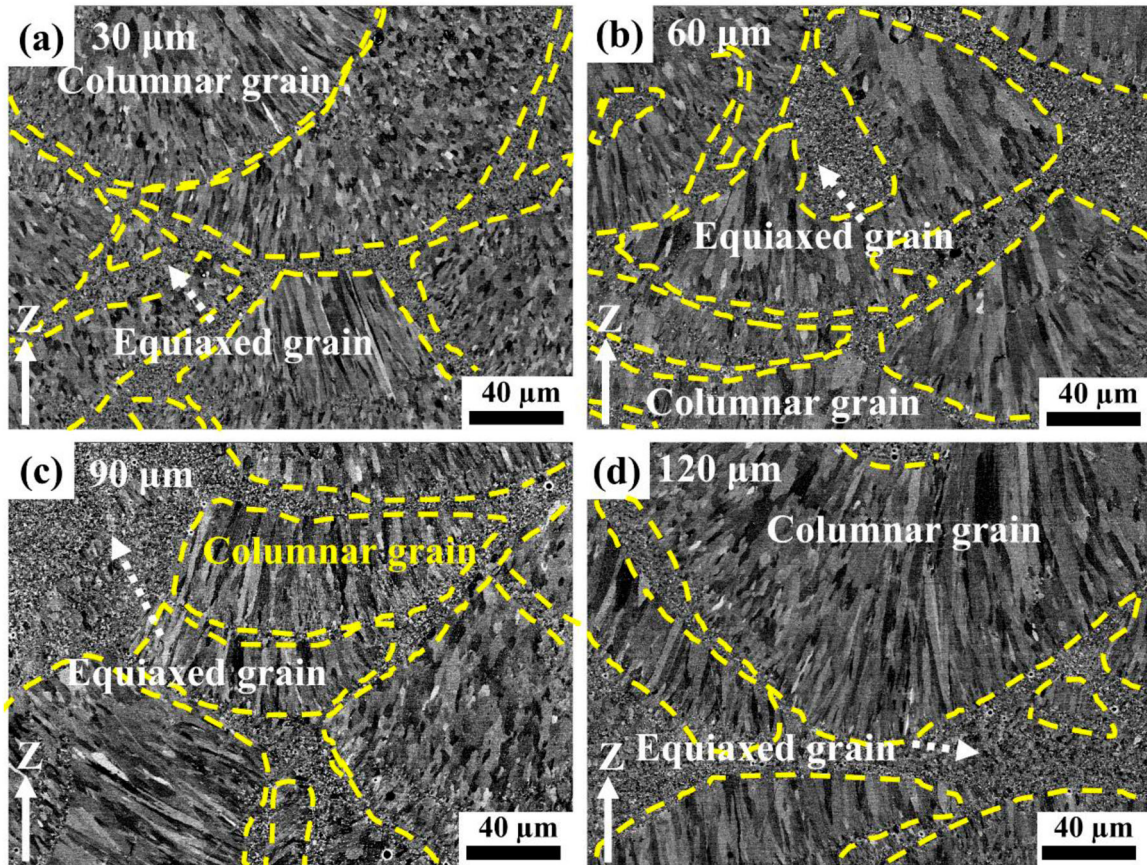


Figure 6. The backscattered electron (BSE) SEM microstructure of post-heat-treated Al-Mn-Mg-Sc-Zr alloys built at different LPBF layer thickness of: (a) 30 μm, (b) 60 μm, (c) 90 μm, and (d) 120 μm. These BSE images were collected on vertical cross-sections which was parallel to the LPBF build direction (Z).

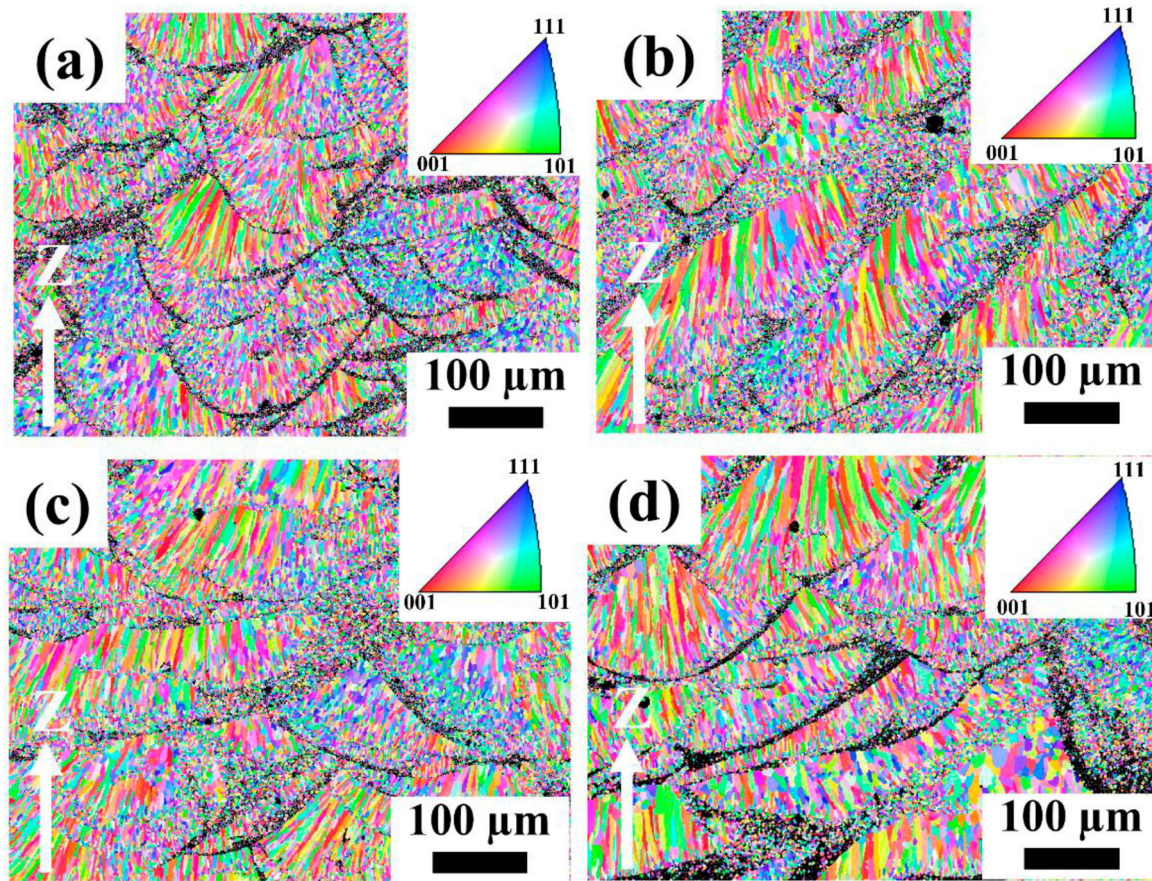


Figure 7. Grain orientation maps show the heterogeneous microstructures of post-heat-treated specimens built at different LPBF layer thickness of: (a) 30 μm , (b) 60 μm , (c) 90 μm , and (d) 120 μm . These maps were collected on vertical cross-sections which was parallel to the LPBF build direction (Z).

High-resolution TEM (HRTEM) was then used to investigate the nano-scale microstructures. Figure 9 shows that a high density of nano precipitates with a diameter below 4 nm in all layer thickness conditions after the post-process heat treatment. According to the fast Fourier transformation (FFT) pseudo-diffractions, these nano precipitates were secondary Al_3Sc with a $\text{L}1_2$ crystal structure [40]. In addition, there was no evident difference in the amount and size of secondary Al_3Sc for different layer thicknesses.

3.4. Mechanical properties

Figure 10(a) shows the representative engineering stress–strain curves of the post-heat-treated Al–Mn–Mg–Sc–Zr alloy built at different LPBF layer thickness,

and their mechanical properties are summarised in Table 4. With increased layer thickness, the post-heat-treated specimens possessed a slightly decreased YS. The samples of 30, 60, 90, and 120 μm exhibited YS of 502 ± 4 MPa, 491 ± 8 MPa, 484 ± 5 MPa and 472 ± 4 MPa, respectively. The decrement in YS was only 6% between the 30 and 120 μm specimens. This decreasing trend with layer thickness was similar in UTS. The fracture strain (ϵ_f) was the highest at $13.1\% \pm 2.7\%$ in the 30 μm specimen, and it reduced to $\sim 10\text{--}11\%$ at the larger layer thickness. This is probably attributed to the increase in defect level and size (Figure 3) at higher layer thickness. Figure 10(b)–(e) shows the tensile fractured surface of 30 and 120 μm specimens. In both specimens, there were intergranular fractured region and dimpled regions,

Table 3. The size and volume fraction of equiaxed grains (EGs), columnar grains (CGs), and secondary Al_3Sc precipitates.

Layer thickness	EG size (μm)	EG fraction (%)	CG size (μm)	CG fraction (%)	Secondary Al_3Sc size (nm)
30 μm	0.9 ± 0.2	20.1 ± 1.0	1.5 ± 0.2	79.9 ± 1.0	2.7 ± 0.5
60 μm	1.2 ± 0.3	22.4 ± 0.4	1.8 ± 0.4	77.6 ± 0.4	2.6 ± 0.6
90 μm	1.6 ± 0.2	28.3 ± 0.7	2.3 ± 0.6	71.3 ± 0.7	2.5 ± 0.7
120 μm	2.1 ± 0.4	29.4 ± 0.4	4.2 ± 1.1	70.6 ± 0.4	2.6 ± 0.5

Notes: The results were measured based on SEM-BSE images in Figure 6 and HRTEM images in Figure 9. The volume fraction of EGs and CGs was determined by using an Image Pro software on SEM-BSE images.

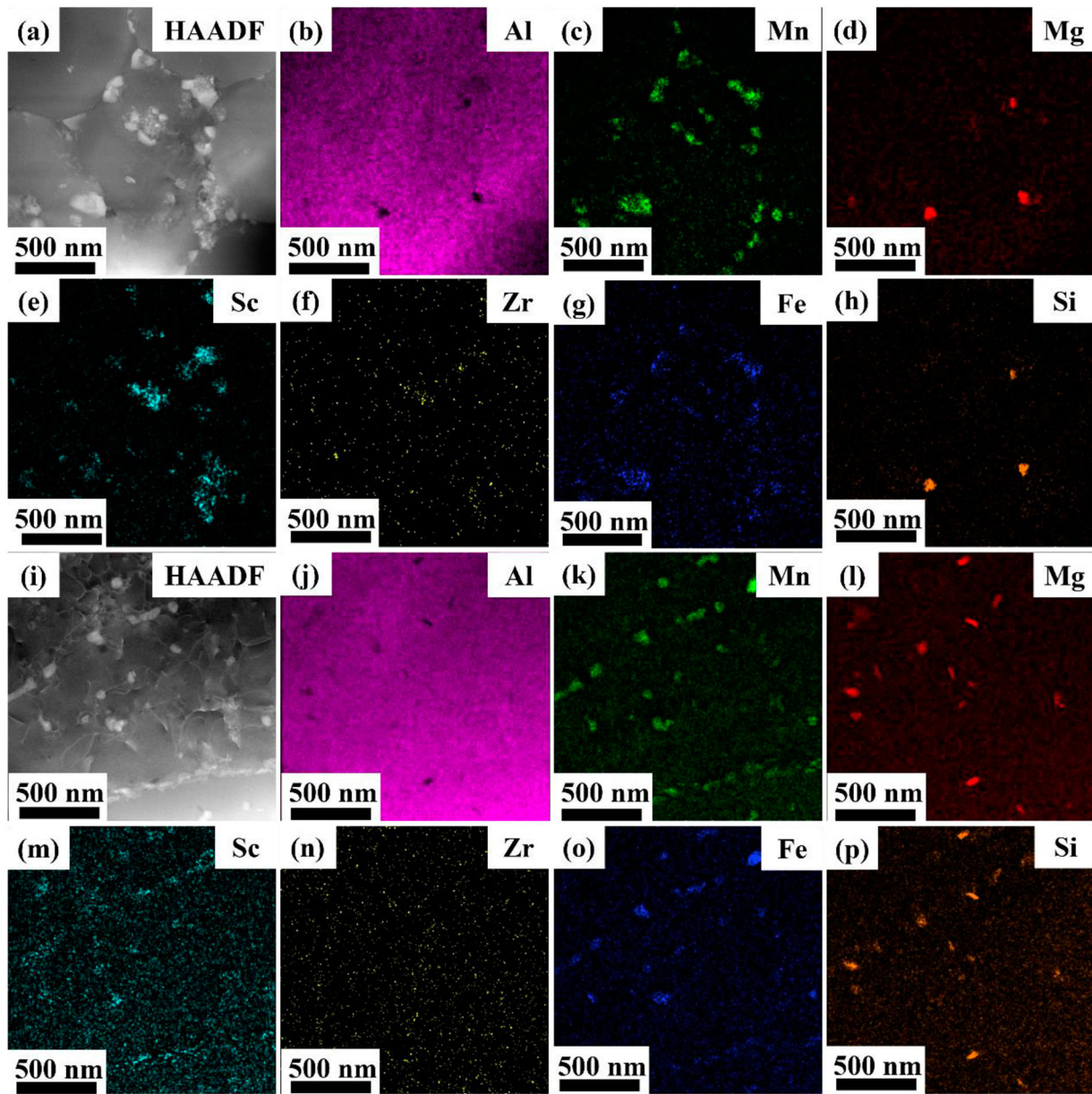


Figure 8. HAADF STEM images and EDS element maps of the post-process heat treated Al-Mn-Mg-Sc-Zr specimen built at a 30 μm layer thickness in: (a)-(h) an equiaxed grain (EG) region, and (i)-(p) a columnar grain (CG) region.

which were correlated to the columnar grains and equiaxed grains, respectively. In addition, defects of micropores and associated microcracks were observed on the fracture surface of specimens built at large layer thickness, as shown in Figure 10(e).

4. Discussion

4.1. Optimal LPBF processing window

In this work, optimal processing windows at different layer thickness were determined for LPBF fabricated Al-Mn-Mg-Sc-Zr alloy. The relative density of the optimised samples was higher than 99% in all layer thickness

conditions according to the image analyses in Table 2 and $\mu\text{-CT}$ results in Figure 3. The $\mu\text{-CT}$ results showed that the relative density decreased from 99.8% in the 30 μm specimen to 99.2% in the 120 μm specimen. For all layer thickness conditions, keyhole defects were observed at high laser powers and low scan speeds as a result of high energy input and associated liquid overheating and evaporation. In contrast, irregular lack-of-fusion defects appeared at low laser powers and high scan speeds due to insufficient energy input. These observations are consistent with previous studies on LPBF of different types of alloys [41–44].

With an enhanced layer thickness, the ranges of laser power and scan speed for processing window were

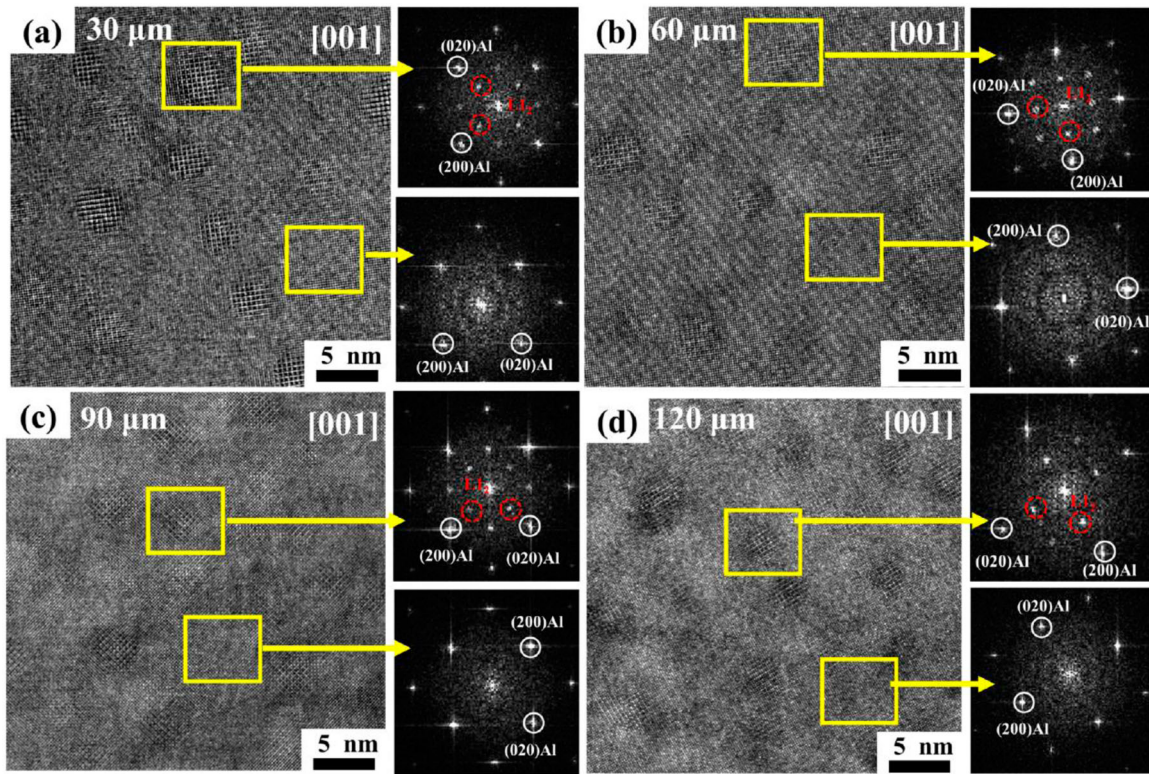


Figure 9. HRTEM images of post-heat-treated Al–Mn–Mg–Sc–Zr alloy samples. The right insets show the [001] fast Fourier transformation (FFTs) from the secondary Al_3Sc nanoparticles and $\alpha\text{-Al}$ matrix for specimens built at different LPBF layer thickness of: (a) 30 μm , (b) 60 μm , (c) 90 μm , (d) 120 μm .

significantly narrowed. This indicates that it is more difficult to obtain an optimal process parameter set at large layer thickness. At a higher layer thickness, it generally required a higher laser power to melt a thicker layer (therefore higher volume) of metallic powder [45]. As shown in Figure 2, the laser power range of processing window increased from 270–370 W for 30 μm to 400–450 W for 120 μm . It is known that high laser powers can effectively increase the maximum temperature within the molten pool [42, 46, 47], and a high peak molten pool temperature induces intensive Marangoni flow and causes the Plateau-Rayleigh instability and balling in turn [46, 48]. Therefore, the processing window range became smaller at a higher layer thickness. In addition, the optimised scan speeds were in the range from 1100 mm/s to 1200 mm/s for the four parameter sets with the highest relative density as highlighted in Table 2. Considering the increased laser powers with the layer thickness, similar scan speeds led to deeper and wider molten pools with a higher depth-to-width ratio at higher layer thickness as shown in Figures 4 and 5.

4.2. LPBF fabrication efficiency

As this work adopted an enhanced layer thickness to improve the LPBF fabrication efficiency, it is necessary

to evaluate the build rates of different layer thickness. By considering the scan speeds, hatch distance, and layer thickness, the volumetric fabrication rate can be estimated. Figure 11 (a) shows the volumetric build rate in this work and some other LPBF fabricated aluminium alloys. For the specimens with the highest relative density fabricated at the four different layer thickness as listed in Table 2, the build rate increased with the layer thickness, as depicted by the black data-points. To be more specifically, the build rates of 30, 60, 90 and 120 μm specimens were 5.04 mm^3/s , 10.08 mm^3/s , 15.12 mm^3/s and 18.48 mm^3/s , respectively. Compared with other LPBF fabricated aluminium alloys [23, 49–56], it is apparent that the layer thickness can effectively improve the build rate, and the fabrication rates (10–19 mm^3/s) of specimens built with a large layer thickness (>50 μm) in this work are much higher than the fabrication rates ($\leq \sim 8 \text{ mm}^3/\text{s}$) reported in previous studies. It is worth mentioning that Figure 6 had not considered the time of powder re-coating, because the powder re-coating process can be different on different LPBF machines due to the differences in re-coater moving speed, re-coater travelling distance, and re-coating strategy [57]. As a large layer thickness can effectively reduce the powder re-coating frequency and the associated time,

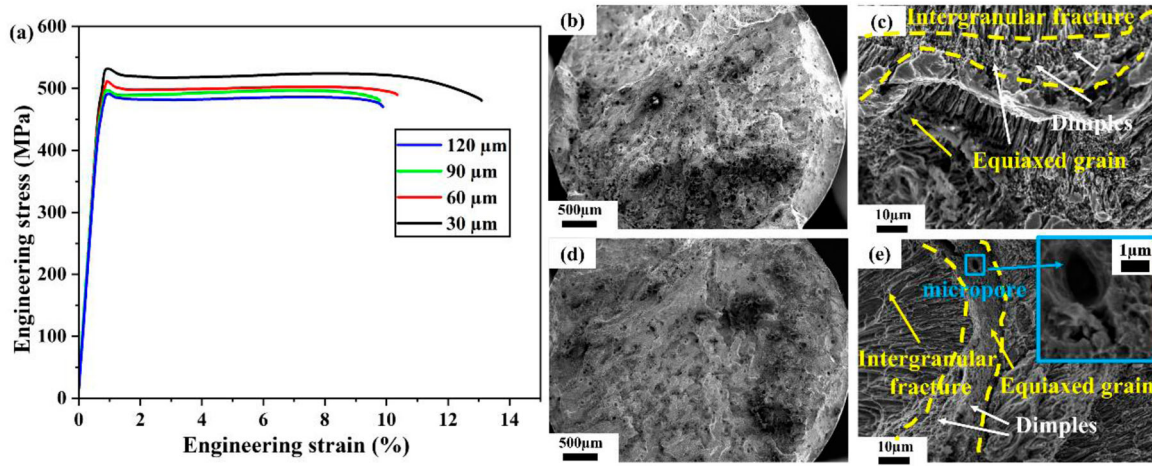


Figure 10. (a) The representative engineering tensile stress-strain curves of post-heat-treated Al-Mn-Sc alloys built at different layer thickness, and the tensile fractured surface of: (b)-(c) 30 μm specimen, and (d)-(e) 120 μm specimen.

the enhanced magnitude in LPBF fabrication rate of the high layer thickness conditions should be even much higher than the estimated values as shown in Figure 11(a).

4.3. Effect of layer thickness on microstructure characteristics

As LPBF is a point-by-point, line-by-line, and layer-by-layer manufacturing process, the morphology and size of melt pool is directly related to the LPBF fabricating parameters [4, 8, 9]. To be more specific, it is known that the laser-matter interactions and heat transfer are complex during the LPBF fabrication process. The microstructural characteristics of Al-Mn-Mg-Sc-Zr alloy are significantly influenced by the cooling rate [6, 58, 59] correlated the cooling rate and melt pool characteristics using the following equation:

$$\frac{\Delta T}{\Delta t} = \frac{\alpha_{\lambda} P_{laser} V^{1/2}}{d^2 (2k\rho c d)^{1/2}} \quad (1)$$

where $\Delta T/\Delta t$ refers to the cooling rate, α_{λ} is the absorptivity at the laser wave length at 0.15 [26], k is the thermal conductivity at 197 W/(m K), ρ is the density at 2.86 g/cm³, and c is the specific heat at 0.89 J/(g K) (k , ρ , and c in this work were calculated using the JMatpro software). In the LPBF process, P_{laser} is the

laser power, V is the scan velocity, and d is the depth of the molten pool. According to the melt pool characteristics in Figure 5, the cooling rates at different layer thicknesses were calculated at 9.8×10^7 , 2.6×10^7 , 2.3×10^7 , and 1.7×10^7 K/s for the 30 μm, 60 μm, 90 μm, and 120 μm specimens, respectively. The estimated cooling rate decreases with the layer thickness, which leads to increased EG and CG size as shown in Table 3.

4.4. The microstructure and property correlation

Figure 11(b) compares the yield strength of post-heat-treated Al-Mn-Mg-Sc-Zr alloys in this work with other LPBF fabricated aluminium alloys with post-process heat treatment in literature [23, 26, 34, 55, 60–68]. In general, the reported LPBF fabricated aluminium alloys were prepared at a layer thickness below 60 μm. In contrast, this work showed that high-strength aluminium alloys can be successfully fabricated at large layer thickness by appropriate LPBF processing parameters. In this work, the samples built at layer thickness of 30, 60, 90, and 120 μm achieved yield strength of 502 ± 4 MPa, 491 ± 8 MPa, 484 ± 5 MPa, and 472 ± 4 MPa after an aging treatment for 5 h at 300 (°C). There was a slight decrease of 6% in yield strength from 30 to 120 μm specimens. The reasons for yield strength decrement were analysed from the following aspects.

4.4.1. The influence of porosity

With an enhanced layer thickness, the porosity level slightly increased from 0.2% at 30 μm to 0.8% at 120 μm layer thickness according to Table 2 and Figure 3. It was reported that a small volume of pores (<1%) did not have an apparent effect on yield strength [69]. Considering the μ -CT results showing these pores

Table 4. Tensile properties the LPBF post-heat-treated Al-Mn-Mg-Sc-Zr alloys built at different LPBF layer thickness.

Layer thickness	YS (MPa)	UTS (MPa)	ϵ_f (%)
30 μm	502 ± 4	527 ± 4	13.1 ± 2.7
60 μm	491 ± 8	513 ± 2	10.7 ± 0.8
90 μm	484 ± 5	502 ± 4	10.3 ± 1.0
120 μm	472 ± 4	495 ± 2	9.8 ± 0.3

Note: Errors are the standard deviations. YS: yield strength; UTS: ultimate tensile strength; ϵ_f : fracture strain.

were non-irregular defects with a low stress concentration, 0.8% pores in the 120 μm sample would have a negligible influence on the yield strength. However, such a small fraction of pores could influence the ductility [70]. As shown in Figure 10(e), cracks formed around the micropores, which then deteriorated the ductility. Therefore, the fracture strain decreased from 30 to 120 μm layer thickness due to the increased volume fraction of pores.

4.4.2. Precipitation hardening

After the post-process heat treatment, the size of both precipitates were large ($\text{Al}_3\text{X} > 70$ nm and $\text{Al}_6(\text{Mn}, \text{Fe}) > 35$ nm). Therefore, in this work, the contribution to the precipitation hardening should be mainly from the secondary Al_3Sc nanoprecipitates with size at below 4 nm [26, 55, 71]. The precipitation of secondary Al_3Sc precipitates (Figure 9) caused by post-heat-treatment is known to have a significant impact on the LPBF fabricated Al-Mn-Mg-Sc-Zr alloy [72]. For precipitates with grain size below 8 nm, they are sheared by dislocations rather than bypassed through Orowan dislocation looping mechanism [73–75]. Considering that the 30, 60, 90, and 120 μm specimens contained secondary Al_3Sc precipitates with average diameters below 4 nm, the precipitation hardening effect can be evaluated as [76]:

$$\sigma_{ppt} = 0.0055M(\Delta G)^{\frac{3}{2}} \left(\frac{2f_v}{G} \right)^{\frac{1}{2}} \left(\frac{r}{b} \right)^{\left(\frac{3}{2}m - 1 \right)} \quad (2)$$

where $M = 3.06$ is the mean matrix orientation factor for aluminium, $G = 25.4$ GPa is the shear modulus of Al, r is the average precipitates radius as shown in Table 3, $b = 0.286$ nm is the matrix Burgers vector, $\Delta G = 42.6$ GPa is

the shear modulus difference between the Al matrix and secondary Al_3Sc precipitates, m is a constant at 0.85 [75] and f_v is the volume fraction of precipitates (1.22 Vol.%, 1.19 Vol.%, 1.16 Vol.% and 1.18 Vol.% for 30, 60, 90 and 120 μm , respectively). As the radius and volume fraction of secondary Al_3Sc precipitates were similar at different layer thickness, the σ_{ppt} were calculated to be 222 MPa, 220 MPa, 218 MPa, and 220 MPa for 30, 60, 90 and 120 μm , respectively. Therefore, the contribution of σ_{ppt} to the yield strength difference at various layer thickness is negligible.

4.4.3. Solid solution strengthening

In general, the amount of Sc and Zr remaining in solid solution presumably has a negligible contribution to the solid solution strengthening in LPBF fabricated Al-Mn-Mg-Sc-Zr alloys [77]. With the help of the ultrafast cooling rate in the LPBF process, an unconventionally high amount of Mn and Mg was placed into solid solution [26]. The substantially different atomic size and shear modulus of Mn and Mg atoms compared to the surrounding Al atoms in the matrix can generate localised strain fields that interact with and hinder dislocations from moving freely through the lattice, thereby increase the yield strength of the material [78]. As a result, only Mn and Mg are considered in the contribution of solid solution strengthening. The yield strength increases owing to the solid solution can be estimated using the equation [78]

$$\sigma_{ss} = \sum A_i C_i^{B_i} \quad (3)$$

where C_i is the concentration of the solute in atomic percentage (Mn and Mg, as shown in Figure 12), A_i is a strengthening coefficient, and B_i is a concentration

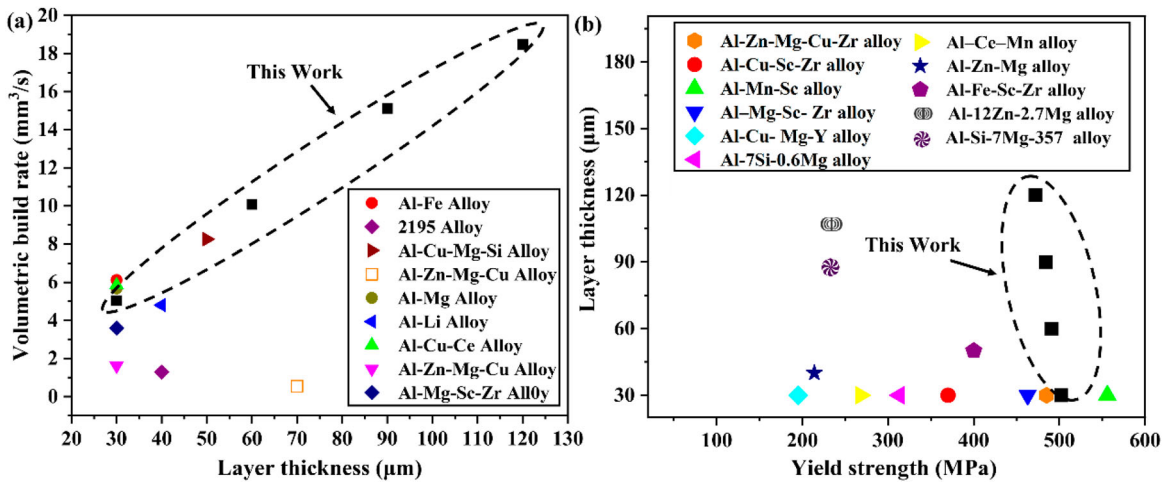


Figure 11. (a) Volumetric build rate of the Al-Mn-Mg-Sc-Zr alloy fabricated in this work compared with other LPBF fabricated aluminium alloys [23, 49–56]; (b) comparison of the yield strength of post-heat-treated Al-Mn-Mg-Sc-Zr alloy built at different layer thickness with other LPBF fabricated aluminium alloys [14, 17, 25, 46, 49–57].

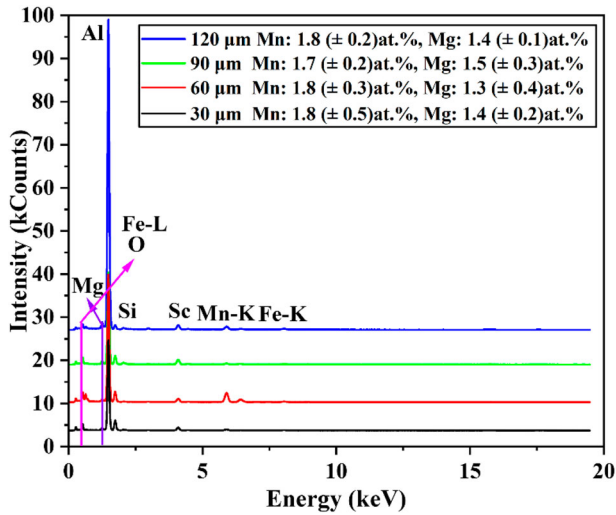


Figure 12. EDS element spectra for α -Al matrix (EDS collection locations were highlighted by the yellow boxes from Figure 9) in the post-heat-treated Al–Mn–Mg–Sc–Zr specimens built at different layer thickness. The atomic concentration of Mn and Mg were estimated from Mn-K and Mg-K peaks.

exponent. Both A_i and B_i depend on the solute species, and were estimated in Ref. [79]. Based on Equation (3) and atomic concentrations in Figure 12, the solid solution strengthening contributions from Mn and Mg are 116, 115, 112 and 116 MPa for 30, 60, 90, and 120 μm , respectively.

4.4.4. Grain boundary strengthening

With an enhanced layer thickness, the grain size of EGs and CGs increased as shown in Table 3. As volume fractions of EGs and CGs changed at different layer thickness, their strengthening effect can be estimated by using a modified linear rule of mixture of Hall-Petch equation [26]:

$$\sigma_{gb} = \sigma_0 + kf_{eg}d_{eg}^{-1/2} + kf_{cg}d_{cg}^{-1/2} \quad (4)$$

where σ_0 is the friction stress of the lattice to dislocation motion (20 MPa for aluminium), k is the Hall-Petch coefficient (0.17 MPa $\text{m}^{1/2}$ for aluminium), d_{eg} and f_{eg} are the average grain size and fraction of equiaxed grains, d_{cg} and f_{cg} are the average grain size and fraction of columnar grains in Table 3. The calculated σ_{gb} are 167, 152, 130 and 110 MPa for 30, 60, 90, and 120 μm specimens, respectively.

The interactions among distinctive strengthening mechanisms are typically very complicated and diverse superposition laws were proposed in this work. It was previously reported that dislocations in high-strength Al–Mn–Mg–Sc–Zr alloys are very limited [77] and the mechanism of dislocation enhancement is not included here. Therefore, considering the precipitation hardening,

Table 5. Calculated strength contribution from different strengthening mechanisms at different LPBF layer thicknesses comparing with the experimental tensile yield strength.

Layer thicknesses	30 μm	60 μm	90 μm	120 μm
σ_{ppt}	222	220	218	220
σ_{ss}	116	115	112	116
σ_{gb}	167	152	137	110
$\sigma_{0.2\text{-estimated}}$	505	487	467	446
$\sigma_{0.2\text{-experimental}}$	502	491	484	472

solid solution strengthening and grain boundary strengthening, the estimated yield strength can be determined at:

$$\sigma_{0.2\text{-estimate}} = \sigma_{ppt} + \sigma_{ss} + \sigma_{gb} \quad (5)$$

the estimated yield strengths (Table 5) are 505, 487, 467, 446 MPa for Al–Mn–Mg–Sc–Zr alloy 30, 60, 90, and 120 μm , respectively. The slight decreasing trend in yield strength estimation well agreed with the tensile test results. The contributions from precipitation hardening and solid solution strengthening are similar at different layer thickness. The dominant contribution to the yield strength decrement is the decreased grain boundary strengthening due to larger grain size at higher layer thickness. Therefore, grain boundary strengthening should be the main cause of the overall difference in yield strength at different layer thicknesses.

In addition, the decreased elongation was mainly related to the increased porosity level at high layer thickness. Nevertheless, a strong (YS of 472 MPa) and ductile (ϵ_f of 9.8%) LPBF fabricated Al–Mn–Mg–Sc–Zr alloy has been achieved at an extremely large layer thickness of 120 μm . This work provides an effective route to produce strong and ductile Al–Mn–Mg–Sc–Zr alloy using fabrication-rate enhanced laser powder bed fusion.

5. Conclusions

The processing optimisation were systematically investigated in LPBF fabricated Al–Mn–Mg–Sc–Zr alloy built at various layer thickness, i.e. 30, 60, 90, and 120 μm . The microstructure and mechanical properties were investigated in the LPBF optimised and heat-treated specimens. The following conclusions can be drawn for this work.

- (1) High relative density ($\geq 99.2\%$) was achieved in all layer thickness conditions. The specimen built at 120 μm layer thickness possessed a 99.2% relative density. Small fraction of defects was generally randomly distributed in the specimen.
- (2) The LPBF fabricated and post-heat-treated Al–Mn–Mg–Sc–Zr alloy had a typical bimodal equiaxed-columnar microstructure. The size of equiaxed grains and columnar grains slightly increased with

the layer thickness, which was attributed to the reduced cooling rate at high layer thicknesses.

- (3) In the post-heat-treated specimens, the yield strength decreased by 6% from 30 μm (502 MPa) to 120 μm (472 MPa). This decrement was mainly attributed to the increased grain size at high layer thicknesses rather than the porosity, solid solution strengthening and precipitation hardening. The reduced fraction strain was caused by the slightly higher porosity levels at high layer thickness.
- (4) This work provides an effective way to produce strong (yield strength at 472 MPa) and ductile (elongation at 9.8%) Al–Mn–Mg–Sc–Zr alloy using fabrication-rate enhanced LPBF at a 120 μm layer thickness.

Disclosure statement

No potential conflict of interest was reported by the author(s).

Funding

The authors thank the financial support from the National Key R&D Program of China (grant number 2022YFB4601000), the National Natural Science Foundation of China (grant number 52204391), the Special Fund Project for Science and Technology Innovation Strategy of Guangdong Province (grant number STKJ2021025, grant number STKJ202209021 & grant number STKJ2023040), the Characteristic Innovation Project (Natural Science) for Regular University in Guangdong Province (grant number 2022KTSCX038), and Shantou University Research Foundation for Talents (grant number NTF21013).

References

- [1] Wang Z, Wang X, Chen X, et al. Complete columnar-to-equiaxed transition and significant grain refinement in an aluminium alloy by adding Nb particles through laser powder Bed fusion. *Addit Manuf.* 2022;51:102615. doi:10.1016/j.addma.2022.102615.
- [2] Chen L-Y, Liang S-X, Liu Y, et al. Additive manufacturing of metallic lattice structures: unconstrained design, accurate fabrication, fascinated performances, and challenges. *Mater Sci Eng: R: Rep.* 2021;146:100648. doi:10.1016/j.mser.2021.100648.
- [3] Xiao Z, Yu W, Fu H, et al. Recent progress on microstructure manipulation of aluminium alloys manufactured via laser powder Bed fusion. *Virtual Phys Prototyp.* 2023;18(1). doi:10.1080/17452759.2022.2125880.
- [4] Wang J, Zhu R, Liu Y, et al. Understanding melt pool characteristics in laser powder bed fusion: an overview of single- and multi-track melt pools for process optimization. *Adv Powder Mater.* 2023;2(4):100137. doi:10.1016/j.apmate.2023.100137.
- [5] Zhang Z, Sun J, Xia J, et al. Corrosion behavior of laser powder Bed fusion Al–Mn–Mg–Sc–Zr alloy on different planes. *SSRN Electronic J.* 2022b;208:110634. doi:10.2139/ssrn.4085262.
- [6] Li Q, Li G, Lin X, et al. Development of a high strength Zr/Sc/Hf-modified Al–Mn–Mg alloy using laser powder Bed fusion: design of a heterogeneous microstructure incorporating synergistic multiple strengthening mechanisms. *Addit Manuf.* 2022;57:102967. doi:10.1016/j.addma.2022.102967.
- [7] Kotadia HR, Gibbons G, Das A, et al. A review of laser powder Bed fusion additive manufacturing of aluminium alloys: microstructure and properties. *Addit Manuf.* 2021;46:102155. doi:10.1016/j.addma.2021.102155.
- [8] Lim CH, Li H, Krishnan M, et al. Novel method of residual stress reduction for AlSi10Mg manufactured using selective laser melting without compromise of mechanical strength. *Virtual Phys Prototyp.* 2023;18(1):4. doi:10.1080/17452759.2022.2131583.
- [9] Tang Z, Wei Q, Gao Z, et al. 2000W blue laser directed energy deposition of AlSi7Mg: process parameters, molten pool characteristics, and appearance defects. *Virtual Phys Prototyp.* 2023;18(1):3. doi:10.1080/17452759.2022.2120405.
- [10] Schuster M, De Luca A, Widmer R, et al. Processability, microstructure and precipitation of a Zr-modified 2618 aluminium alloy fabricated by laser powder bed fusion. *J Alloys Compd.* 2022;913:165346. doi:10.1016/j.jallcom.2022.165346.
- [11] Zhou L, Hyer H, Park S, et al. Microstructure and mechanical properties of Zr-modified aluminum alloy 5083 manufactured by laser powder Bed fusion. *Addit Manuf.* 2019;28:485–496. doi:10.1016/j.addma.2019.05.027.
- [12] Opprecht M, Garandet J-P, Roux G, et al. An understanding of duplex microstructures encountered during high strength aluminium alloy laser beam melting processing. *Acta Mater.* 2021;215:117024. doi:10.1016/j.actamat.2021.117024.
- [13] Zhou SY, Su Y, Wang H, et al. Selective laser melting additive manufacturing of 7xxx series Al–Zn–Mg–Cu alloy: cracking elimination by Co-incorporation of Si and TiB₂. *Addit Manuf.* 2020;36:101458. doi:10.1016/j.addma.2020.101458.
- [14] Yang F, Wang J, Wen T, et al. Developing a novel high-strength Al–Mg–Zn–Si alloy for laser powder Bed fusion. *Mater Sci Eng A.* 2022;851:143636. doi:10.1016/j.msea.2022.143636.
- [15] Babu AP, Lam MC, Ma J, et al. Influence of second phase particles on the mechanical properties of a high solute Al–Zn–Mg alloy fabricated through laser powder Bed fusion. *J Alloys Compd.* 2022;897:162958. doi:10.1016/j.jallcom.2021.162958.
- [16] Rakhmonov JU, Weiss D, Dunand DC. Solidification microstructure, aging evolution and creep resistance of laser powder-Bed fused Al–7Ce–8Mg (Wt%). *Addit Manuf.* 2022;55:102862. doi:10.1016/j.addma.2022.102862.
- [17] Chen Y, Xiao C, Zhu S, et al. Microstructure characterization and mechanical properties of crack-free Al–Cu–Mg–Y alloy fabricated by laser powder Bed fusion. *Addit Manuf.* 2022;58:103006. doi:10.1016/j.addma.2022.103006.
- [18] Yu SJ, Wang P, Li HC, et al. Heterogeneous microstructure and mechanical behaviour of Al–8.3Fe–1.3V–1.8Si alloy produced by laser powder Bed fusion. *Virtual Phys Prototyp.* 2023;18(1). doi:10.1080/17452759.2022.2155197.

- [19] Spierings AB, Dawson K, Uggowitzer PJ, et al. Influence of SLM scan-speed on microstructure, precipitation of Al₃Sc particles and mechanical properties in Sc- and Zr-modified Al-Mg alloys. *Mater Des.* 2018;140:134–143. doi:10.1016/j.matdes.2017.11.053.
- [20] Geng Y, Tang H, Xu J, et al. Strengthening mechanisms of high-performance Al-Mn-Mg-Sc-Zr alloy fabricated by selective laser melting. *Sci China Mater.* 2021;64(12):3131–3137. doi:10.1007/s40843-021-1719-8.
- [21] Zhu Z, Ng FL, Seet HL, et al. Superior mechanical properties of a selective-laser-melted AlZnMgCuScZr alloy enabled by a tunable hierarchical microstructure and dual-nanoprecipitation. *Mater Today.* 2022;52:90–101. doi:10.1016/j.mattod.2021.11.019.
- [22] Tang H, Geng Y, Bian S, et al. An ultra-high strength over 700 MPa in Al-Mn-Mg-Sc-Zr alloy fabricated by selective laser melting. *Acta Metallurgica Sinica (English Letters).* 2022;35(3):466–474. doi:10.1007/s40195-021-01286-2.
- [23] Wang P, Gammer C, Brenne F, et al. Microstructure and mechanical properties of a heat-treatable Al-3.5Cu-1.5Mg-1Si alloy produced by selective laser melting. *Mater Sci Eng A.* 2018;711:562–570. doi:10.1016/j.msea.2017.11.063.
- [24] Wang Y, Lin X, Zhao Y, et al. Laser powder Bed fusion of Zr-modified Al-Cu-Mg alloy: processability and elevated-temperature mechanical properties. *J Mater Sci Technol.* 2022b;136:223–235. doi:10.1016/j.jmst.2022.07.027.
- [25] Jia Q, Rometsch P, Cao S, et al. Towards a high strength aluminium alloy development methodology for selective laser melting. *Mater Des.* 2019a;174:107775. doi:10.1016/j.matdes.2019.107775.
- [26] Jia Q, Rometsch P, Kürnstner P, et al. Selective laser melting of a high strength Al[sbnd]Mn[sbnd]Sc alloy: alloy design and strengthening mechanisms. *Acta Mater.* 2019b;171:108–118. doi:10.1016/j.actamat.2019.04.014.
- [27] Rometsch P, Jia Q, Yang KV, et al. Aluminum alloys for selective laser melting - towards improved performance. *Addit Manuf Aerosp Ind.* 2019; 301–325. doi:10.1016/B978-0-12-814062-8.00016-9.
- [28] Jia Q, Zhang F, Rometsch P, et al. Precipitation kinetics, microstructure evolution and mechanical behavior of a developed Al-Mn-Sc alloy fabricated by selective laser melting. *Acta Mater.* 2020;193:239–251. doi:10.1016/j.actamat.2020.04.015.
- [29] Schliephake D, Lopes C, Eggeler YM, et al. Improved work hardening capability and ductility of an additively manufactured and deformed Al-Mn-Mg-Sc-Zr alloy. *J Alloys Compd.* 2022;924:166499. doi:10.1016/j.jallcom.2022.166499.
- [30] Mehta B, Nyborg L, Frisk K, et al. Al-Mn-Cr-Zr-based alloys tailored for powder Bed fusion-laser beam process: alloy design, printability, resulting microstructure and alloy properties. *J Mater Res.* 2022;37(6):1256–1268. doi:10.1557/s43578-022-00533-1.
- [31] Lv B, Wang F, Niu X, et al. In-Situ formed graded microstructure and mechanical property of selective laser melted 15–5 PH stainless steel. *Mater Sci Eng A.* 2022;847:143340. doi:10.1016/j.msea.2022.143340.
- [32] Zhao T, Cai W, Dahmen M, et al. Ageing response of an Al-Mg-Mn-Sc-Zr alloy processed by laser metal deposition in thin-wall structures. *Vacuum.* 2018;158:121–125. doi:10.1016/j.vacuum.2018.09.052.
- [33] Babu AP, Kairi SK, Huang A, et al. Laser powder Bed fusion of high solute Al-Zn-Mg alloys: processing, characterisation and properties. *Mater Des.* 2020;196:109183. doi:10.1016/j.matdes.2020.109183.
- [34] Rometsch PA, Zhu Y, Wu X, et al. Review of high-strength aluminium alloys for additive manufacturing by laser powder Bed fusion. *Mater Des.* 2022;219:110779. doi:10.1016/j.matdes.2022.110779.
- [35] Cai C, Wu X, Liu W, et al. Selective laser melting of near- α titanium alloy Ti-6Al-2Zr-1Mo-1V: parameter optimization, heat treatment and mechanical performance. *J Mater Sci Technol.* 2020;57:51–64. doi:10.1016/j.jmst.2020.05.004.
- [36] Chlebus E, Kuźnicka B, Kurzynowski T, et al. Microstructure and mechanical behaviour of Ti-6Al-7Nb alloy produced by selective laser melting. *Mater Charact.* 2011;62(5):488–495. doi:10.1016/j.matchar.2011.03.006.
- [37] Ma M, Wang Z, Gao M, et al. Layer thickness dependence of performance in high-power selective laser melting of 1Cr18Ni9Ti stainless steel. *J Mater Process Technol.* 2015;215(1):142–150. doi:10.1016/j.jmatprotec.2014.07.034.
- [38] Liu YJ, Liu Z, Jiang Y, et al. Gradient in microstructure and mechanical property of selective laser melted AlSi10Mg. *J Alloys Compd.* 2018;735:1414–1421. doi:10.1016/j.jallcom.2017.11.020.
- [39] Vlach M, Stulikova I, Smola B, et al. Precipitation in cold-rolled Al-Sc-Zr and Al-Mn-Sc-Zr alloys prepared by powder metallurgy. *Mater Charact.* 2013;86:59–68. doi:10.1016/j.matchar.2013.09.010.
- [40] Schuster M, De Luca A, Mathur A, et al. Precipitation in a 2xxx series Al-Cu-Mg-Zr alloy fabricated by laser powder Bed fusion. *Mater Des.* 2021;211:110131. doi:10.1016/j.matdes.2021.110131.
- [41] Zhang H, Zhou C, Wei C. Mathematical and physical modeling of metal delivery system during Top side-pouring twin-roll casting. *J Mater Process Technol.* 2018;254:1–12. doi:10.1016/j.jmatprotec.2017.11.016.
- [42] Cao S, Chen Z, Lim CVS, et al. Defect, microstructure, and mechanical property of Ti-6Al-4V alloy fabricated by high-power selective laser melting. *Jom.* 2017;69(12):2684–2692. doi:10.1007/s11837-017-2581-6.
- [43] Zhang LC, Klemm D, Eckert J, et al. Manufacture by selective laser melting and mechanical behavior of a biomedical Ti-24Nb-4Zr-8Sn alloy. *Scr Mater.* 2011;65(1):21–24. doi:10.1016/j.scriptamat.2011.03.024.
- [44] Colombo-Pulgarin JC, Biffi CA, Vedani M, et al. Beta titanium alloys processed by laser powder Bed fusion: a review. *J Mater Eng Perform.* 2021;30(9):6365–6388. doi:10.1007/s11665-021-05800-6.
- [45] Zhang B, Dembinski L, Coddet C. The study of the laser parameters and environment variables effect on mechanical properties of high compact parts elaborated by selective laser melting 316L powder. *Mater Sci Eng A.* 2013;584:21–31. doi:10.1016/j.msea.2013.06.055.
- [46] Cao S, Zou Y, Lim CVS, et al. Review of laser powder Bed fusion (LPBF) fabricated Ti-6Al-4V: process, post-process treatment, microstructure, and property. *Light: Adv Manuf.* 2021;2(3):313–332. doi:10.37188/lam.2021.020.
- [47] Yang J, Han J, Yu H, et al. Role of molten pool mode on formability, microstructure and mechanical properties

- of selective laser melted Ti-6Al-4V alloy. *Mater Des.* **2016**;110:558–570. doi:[10.1016/j.matdes.2016.08.036](https://doi.org/10.1016/j.matdes.2016.08.036).
- [48] Abd-Elaziem W, Elkattany S, Abd-Elaziem A-E, et al. On the current research progress of metallic materials fabricated by laser powder Bed fusion process: a review. *J Mater Res Technol.* **2022**;20:681–707. doi:[10.1016/j.jmrt.2022.07.085](https://doi.org/10.1016/j.jmrt.2022.07.085).
- [49] Qi Y, Zhang H, Nie X, et al. A high strength Al–Li alloy produced by laser powder Bed fusion: densification, microstructure, and mechanical properties. *Addit Manuf.* **2020b**;35:101346. doi:[10.1016/j.addma.2020.101346](https://doi.org/10.1016/j.addma.2020.101346).
- [50] Rasch M, Heberle J, Dechet MA, et al. Grain structure evolution of Al–Cu alloys in powder Bed fusion with laser beam for excellent mechanical properties. *Materials (Basel).* **2020**;13(1). doi:[10.3390/ma13010082](https://doi.org/10.3390/ma13010082).
- [51] Wang P, Li HC, Prashanth KG, et al. Selective laser melting of Al–Zn–Mg–Cu: heat treatment, microstructure and mechanical properties. *J Alloys Compd.* **2017**;707:287–290. doi:[10.1016/j.jallcom.2016.11.210](https://doi.org/10.1016/j.jallcom.2016.11.210).
- [52] Qi X, Takata N, Suzuki A, et al. Laser powder Bed fusion of a near-eutectic Al–Fe binary alloy: processing and microstructure. *Addit Manuf.* **2020a**;35:101308. doi:[10.1016/j.addma.2020.101308](https://doi.org/10.1016/j.addma.2020.101308).
- [53] Zhou Z, Chen J, Wen F, et al. Optimization of heat treatment for an Al–Mg–Sc–Mn–Zr alloy with ultrafine grains manufactured by laser powder Bed fusion. *Mater Charact.* **2022**;189:111977. doi:[10.1016/j.matchar.2022.111977](https://doi.org/10.1016/j.matchar.2022.111977).
- [54] Bahl S, Sisco K, Yang Y, et al. Al–Cu–Ce(–Zr) alloys with an exceptional combination of additive processability and mechanical properties. *Addit Manuf.* **2021**;48:102404. doi:[10.1016/j.addma.2021.102404](https://doi.org/10.1016/j.addma.2021.102404).
- [55] Liu X, Liu Y, Zhou Z, et al. Enhanced strength and ductility in Al–Zn–Mg–Cu alloys fabricated by laser powder Bed fusion using a synergistic grain-refining strategy. *J Mater Sci Technol.* **2022a**;124:41–52. doi:[10.1016/j.jmst.2021.12.078](https://doi.org/10.1016/j.jmst.2021.12.078).
- [56] Wang Z, Lin X, Kang N, et al. Strength–Ductility synergy of selective laser melted Al–Mg–Sc–Zr alloy with a heterogeneous grain structure. *Addit Manuf.* **2020**;34:101260. doi:[10.1016/j.addma.2020.101260](https://doi.org/10.1016/j.addma.2020.101260).
- [57] King WE, Barth HD, Castillo VM, et al. Observation of keyhole-mode laser melting in laser powder-Bed fusion additive manufacturing. *J Mater Process Technol.* **2014**;214(12):2915–2925. doi:[10.1016/j.jmatprotec.2014.06.005](https://doi.org/10.1016/j.jmatprotec.2014.06.005).
- [58] Buchbinder D, Schleifenbaum H, Heidrich S, et al. High power selective laser melting (HP SLM) of aluminum parts. *Phys Procedia.* **2011**;12:271–278. doi:[10.1016/j.phpro.2011.03.035](https://doi.org/10.1016/j.phpro.2011.03.035).
- [59] Hofmeister W, Griffith M, Ensz M, et al. Solidification in direct metal deposition by LENS processing. *Jom.* **2001**;53(9):30–34. doi:[10.1007/s11837-001-0066-z](https://doi.org/10.1007/s11837-001-0066-z).
- [60] Zhang H, Gu D, Dai D, et al. Influence of scanning strategy and parameter on microstructural feature, residual stress and performance of Sc and Zr modified Al–Mg alloy produced by selective laser melting. *Mater Sci Eng A.* **2020**;788:139593. doi:[10.1016/j.msea.2020.139593](https://doi.org/10.1016/j.msea.2020.139593).
- [61] Aboulkhair NT, Simonelli M, Parry L, et al. 3D printing of aluminium alloys: additive manufacturing of aluminium alloys using selective laser melting. *Prog Mater Sci.* **2019**;106:100578. doi:[10.1016/j.pmatsci.2019.100578](https://doi.org/10.1016/j.pmatsci.2019.100578).
- [62] Mehta A, Zhou L, Huynh T, et al. Additive manufacturing and mechanical properties of the dense and crack free Zr-modified aluminum alloy 6061 fabricated by the laser-powder Bed fusion. *Addit Manuf.* **2021**;41:101966. doi:[10.1016/j.addma.2021.101966](https://doi.org/10.1016/j.addma.2021.101966).
- [63] Wang T, Wang Y, Yang X, et al. Cracks and process control in laser powder Bed fusion of Al–Zn–Mg alloy. *J Manuf Process.* **2022a**;81:571–579. doi:[10.1016/j.jmapro.2022.06.066](https://doi.org/10.1016/j.jmapro.2022.06.066).
- [64] Liu X, Liu Y, Zhou Z, et al. A combination strategy for additive manufacturing of AA2024 high-strength aluminium alloys fabricated by laser powder Bed fusion: role of hot isostatic pressing. *Mater Sci Eng A.* **2022b**;850:143597. doi:[10.1016/j.msea.2022.143597](https://doi.org/10.1016/j.msea.2022.143597).
- [65] Wang Y, Li R, Yuan T, et al. Microstructure and mechanical properties of Al–Fe–Sc–Zr alloy additively manufactured by selective laser melting. *Mater Charact.* **2021**;180:111397. doi:[10.1016/j.matchar.2021.111397](https://doi.org/10.1016/j.matchar.2021.111397).
- [66] Kimura T, Nakamoto T, Ozaki T, et al. Microstructural development and aging behavior of Al–Cr–Zr heat-resistant alloy fabricated using laser powder Bed fusion. *J Mater Res Technol.* **2021**;15:4193–4207. doi:[10.1016/j.jmrt.2021.10.027](https://doi.org/10.1016/j.jmrt.2021.10.027).
- [67] Bayoumy D, Schliephake D, Dietrich S, et al. Intensive processing optimization for achieving strong and ductile Al–Mn–Mg–Sc–Zr alloy produced by selective laser melting. *Mater Des.* **2021**;198:15–17. doi:[10.1016/j.matdes.2020.109317](https://doi.org/10.1016/j.matdes.2020.109317).
- [68] Zhang B, Wei W, Shi W, et al. Effect of heat treatment on the microstructure and mechanical properties of Er-containing Al–7Si–0.6 Mg alloy by laser powder Bed fusion. *J Mater Res Technol.* **2022a**;18:3073–3084. doi:[10.1016/j.jmrt.2022.04.023](https://doi.org/10.1016/j.jmrt.2022.04.023).
- [69] Cordova L, Bor T, Marc de S, et al. Effects of powder reuse on the microstructure and mechanical behaviour of Al–Mg–Sc–Zr alloy processed by laser powder Bed fusion (LPBF). *Addit Manuf.* **2020**;36:101625. doi:[10.1016/j.addma.2020.101625](https://doi.org/10.1016/j.addma.2020.101625).
- [70] Yadroitsev I, Yadroitsava I, Bertrand P, et al. Factor analysis of selective laser melting process parameters and geometrical characteristics of synthesized single tracks. *Rapid Prototyp J.* **2012**;18(3):201–208. doi:[10.1108/13552541211218117](https://doi.org/10.1108/13552541211218117).
- [71] Agrawal P, Gupta S, Thapliyal S, et al. Additively manufactured novel Al–Cu–Sc–Zr alloy: microstructure and mechanical properties. *Addit Manuf.* **2021**;37:101623. doi:[10.1016/j.addma.2020.101623](https://doi.org/10.1016/j.addma.2020.101623).
- [72] Guo Y, Liu B, Xie W, et al. Anti-Phase boundary energy of β series precipitates in Mg–Y–Nd system. *Scr Mater.* **2021**;193:127–131. doi:[10.1016/j.scriptamat.2020.11.004](https://doi.org/10.1016/j.scriptamat.2020.11.004).
- [73] Jawed SF, Rabadia CD, Liu YJ, et al. Strengthening mechanism and corrosion resistance of beta-type Ti–Nb–Zr–Mn alloys. *Mater Sci Eng C.* **2020**;110:110728. doi:[10.1016/j.msec.2020.110728](https://doi.org/10.1016/j.msec.2020.110728).
- [74] Luo X, Liu LH, Yang C, et al. Overcoming the strength–ductility trade-off by tailoring grain-boundary metastable Si-containing phase in β -type titanium alloy. *J Mater Sci Technol.* **2021**;68:112–123. doi:[10.1016/j.jmst.2020.06.053](https://doi.org/10.1016/j.jmst.2020.06.053).
- [75] Fuller CB, Seidman DN, Dunand DC. Mechanical properties of Al(Sc,Zr) alloys at ambient and elevated temperatures. *Acta Mater.* **2003**;51(16):4803–4814. doi:[10.1016/S1359-6454\(03\)00320-3](https://doi.org/10.1016/S1359-6454(03)00320-3).

- [76] Li G, Brodu E, Soete J, et al. Exploiting the rapid solidification potential of laser powder Bed fusion in high strength and crack-free Al-Cu-Mg-Mn-Zr alloys. *Addit Manuf.* **2021**;47:102210. doi:[10.1016/j.addma.2021.102210](https://doi.org/10.1016/j.addma.2021.102210).
- [77] Bayoumy D, Kwak K, Boll T, et al. Origin of Non-uniform plasticity in a high-strength Al-Mn-Sc based alloy produced by laser powder Bed fusion. *J Mater Sci Technol.* **2022**;103:121–133. doi:[10.1016/j.jmst.2021.06.042](https://doi.org/10.1016/j.jmst.2021.06.042).
- [78] Varvenne C, Leyson GPM, Ghazisaeidi M, et al. Solute strengthening in random alloys. *Acta Mater.* **2017**;124:660–683. doi:[10.1016/j.actamat.2016.09.046](https://doi.org/10.1016/j.actamat.2016.09.046).
- [79] Ryen Ø, Nijs O, Sjölander E, et al. “Strengthening mechanisms in solid solution aluminum alloys. *Metall Mater Trans A.* **2006**;37(6):1999–2006. doi:[10.1007/s11661-006-0142-7](https://doi.org/10.1007/s11661-006-0142-7).